



Stress concentration factors in CFRP-reinforced KT-joints under multiplanar bending loads: experimental and numerical investigation

Mohsin Iqbal^{a,*}, Saravanan Karuppanan^a, Veeradasan Perumal^a, Mark Ovinis^b, Afzal Khan^c

^a Mechanical Engineering Department, Universiti Teknologi PETRONAS 32610 Seri Iskandar, Perak, Malaysia

^b College of Engineering, Birmingham City University, Birmingham B4-7XG, UK

^c Department of Mechanical Engineering, University of Engineering and Technology, Peshawar 25120, Pakistan

ARTICLE INFO

Keywords:

Circular hollow section KT-joints
Carbon fibre reinforced polymers reinforcement
Stress concentration factors (SCF)
Empirical models
Artificial neural networks (ANN)

ABSTRACT

Composite materials are widely utilised for rehabilitating critical load-bearing members, including the joints of circular hollow section (CHS) structures, due to their enhanced performance and durability. The accurate prediction of stress concentration factors (SCFs) in CHS joints is challenging because of the complex stress distribution, especially under multiplanar loading conditions. Traditional empirical models predict SCFs only at specific locations, such as the saddle and crown, which are insufficient under multiplanar loading as the maximum SCF can occur elsewhere, potentially leading to inaccuracies in fatigue life estimations. This study aims to address these limitations by developing new empirical models for SCF prediction across the weld toe at the chord-brace interface. A comprehensive finite element analysis was conducted on 10,858 CFRP-reinforced KT-joints with varying configurations under uniplanar, biplanar, and multiplanar bending loads. Artificial neural networks (ANNs) were employed to create empirical models capable of predicting SCFs across diverse load scenarios. The proposed models were validated experimentally on a typical KT-joint, demonstrating a maximum error of less than 15 % at the location of peak SCF. These findings highlight the critical influence of reinforcement properties, such as thickness, orientation and elastic modulus, on SCFs and fatigue life. Future research should focus on enhancing the generalisability of these models to other CHS joints and considering practical factors, including residual stresses from welding and environmental effects like temperature and humidity.

Abbreviation

ANN	Artificial neural networks
API	American Petroleum Institute
CFRP	Carbon fibre-reinforced polymers
CHS	Circular hollow section
FE	Finite element
FEA	Finite element analysis
FRP	Fibre-reinforced polymers
GFRP	Glass fibre-reinforced polymers
HSS	Hot-spot stress
IPB	In-plane bending
MSE	Mean Square Error
OPB	Out-of-plane bending
R^2	Coefficient of determination
SCF	Stress concentration factors

ZPSS	Zero Point Structural Stress
L	Chord length
D	Chord diameter
ϵ	Ratio of the elastic modulus of reinforcement to the elastic modulus of the joint
d	Brace diameter
g	Gap between braces
α	Ratio of twice length to chord diameter
β	Ratio of the brace diameter to the chord diameter
γ	Ratio of chord diameter to twice its thickness
ζ	Ratio of the circumferential gap to the chord diameter
η	Ratio of reinforcement thickness to the chord thickness
Θ	Angle between inclined brace and chord axis
τ	Ratio of brace thickness to chord thickness
ψ	SCF reduction coefficient

* Corresponding author.

E-mail addresses: mohsin_22005143@utp.edu.my (M. Iqbal), saravanan_karuppanan@utp.edu.my (S. Karuppanan), veeradasan.perumal@utp.edu.my (V. Perumal), mark.ovinis@bcu.ac.uk (M. Ovinis), afzalkhan@uetpeshawar.edu.pk (A. Khan).

<https://doi.org/10.1016/j.rineng.2024.103745>

Received 28 October 2024; Received in revised form 13 December 2024; Accepted 13 December 2024

Available online 15 December 2024

2590-1230/© 2024 The Author(s). Published by Elsevier B.V. This is an open access article under the CC BY-NC-ND license (<http://creativecommons.org/licenses/by-nc-nd/4.0/>).

Table 1
Literature on SCFs in bending loaded CHS joints with composite reinforcement.

S. No.	Literature reference	Joint	Load
1.	Hosseini et al. [16]	T/Y-joint	OPB, IPB
2.	Nassiraei et al. [17]	T/Y-joint	IPB
3.	Nassiraei et al. [18]	T/Y-joint	OPB
4.	Nassiraei et al. [19]	X-joint	OPB
5.	Nassiraei et al. [20]	X-joint	OPB
6.	Zavvar et al. [21]	KT-joint	OPB, IPB
7.	Hosseini et al. [22]	T/Y-joint	OPB, IPB
8.	Mohamed et al. [23]	T/Y-joint	OPB, IPB
9.	Rashnooie et al. [24]	T/Y-joint	IPB

1. Introduction

Since the advent of fibre-reinforced polymer (FRP) composites, their usage has grown exponentially. FRPs offer high specific strength and stiffness, ease of application, adaptability to complex geometries, and customizable properties. Beyond their widespread use in aerospace, automotive, sports, and biomedical sectors, FRPs have gained acceptance in the repair and reinforcement of structural elements. Initially, the application of composites in steel structures was limited to environmental protection and the strengthening of secondary elements. Over time, they have been employed to reinforce critical load-bearing structures, providing enhanced structural performance. Zhao et al. [1] reviewed the composite reinforcement of hollow-section steel structures and concluded that composites hold significant potential for retrofitting steel structures. Similarly, Teng et al. [2] demonstrated that the application of composites to existing structures can significantly enhance their fatigue strength.

Joints are the most critical sections in circular hollow section (CHS) structures and often require repair or reinforcement to maintain structural integrity, especially for facilities operating beyond their design life [3]. Such reinforcement may also be needed to comply with revised design codes or new legislative requirements with stricter standards. Iqbal et al. [4] summarised various approaches used for reinforcing CHS joints, identifying composites as a promising alternative for rehabilitating CHS joints. The first documented use of composites for rehabilitating CHS joints was by Pantelides et al. [5]. Since then, various studies have explored the use of composites to strengthen tubular joints under different conditions. Due to the complex variation of stress at the interface of tubular members, analytical modelling is challenging. As a result, numerous studies have explored the performance of composite-reinforced CHS joints under different loading scenarios. The studies focusing on strength enhancement include those by Fam et al. [6], Chen et al. [7], Fu et al. [8], Lesani et al. [9–11], Prashob et al. [12], Alembagheri et al. [13], and Yazdi et al. [14], with a focus on enhancing ultimate load capacity, improving fatigue strength, or reducing stress concentration factors (SCFs). Additionally, parametric equations and probability distribution functions have been developed for various CHS joints [15].

SCFs are widely used to estimate fatigue life through the structural hot-spot stress (HSS) approach, especially during the design phase. However, research on SCFs in CHS joints reinforced with composites has mostly focused on axially loaded joints, as this is the simplest load case. Bending loads on CHS joints can be categorised as in-plane bending (IPB), out-of-plane bending (OPB), or different combinations of these planar loads. A few studies, as summarised in Table 1, have investigated planar bending loads. To our knowledge, multiplanar bending loads, although commonly encountered in practice, have not been investigated [15].

The behaviour of SCFs in CHS joints under multiplanar bending loads differs from that under planar loads. Under simultaneous IPB and OPB, the maximum SCF occurs between the crown and saddle positions,

depending on the relative magnitude of the load components. In contrast, under pure planar loads, the location of maximum SCF is fixed at the crown for IPB and the saddle for OPB [25]. Accurate determination of maximum SCF is essential for reliable fatigue life estimation using HSS and S-N curves. The HSS can be calculated by superimposing stresses based on SCFs and nominal loads in each planar direction [26]. However, this approach requires that the SCFs at various positions in each planar direction are known.

Gulati et al. [27] suggested calculating SCFs at eight specific points, while Iqbal et al. [28,29] and Rasul et al. [30–33] proposed empirical models to determine SCFs at 15-degree intervals. This study builds on these models by developing empirical equations that provide SCFs at every 15°. This enables the HSS to be interpolated across 360° and the peak HSS to be identified. Although recent studies have proposed empirical equations for SCF estimation between the crown and saddle points, various composite-reinforced CHS joint configurations remain unexplored [15]. Furthermore, the optimal orientation of fibre reinforcement under multiplanar loads has rarely been investigated. Recently, Iqbal et al. [34] found that aligning the fibre reinforcement orthogonal to the weld toe results in the greatest reduction in SCF. This study follows the same reinforcement orientation and experimentally validates the findings of Iqbal et al. [34].

Hosseini et al. [16] conducted the first study on SCFs in composite-reinforced CHS joints subjected to IPB and OPB, reporting a significant reduction in the SCF. Nassiraei et al. [17] achieved up to 40 % reduction in SCF in composite-reinforced T/Y-joints subjected to IPB and developed parametric equations for SCF at the heel and toe positions. Subsequently, Nassiraei et al. [18] studied T/Y-joints under OPB, concluding that the reduction in SCF increases with an increase in thickness and elastic modulus of the composite reinforcement, and proposed an equation for SCF at the saddle point. Another study examined CFRP-reinforced X-joints under OPB, reporting a 23 % reduction in SCF [19] and a 37 % reduction in SCF for X-joints under IPB [20].

Zavvar et al. [21] analysed composite-reinforced KT-joints under various IPB and OPB configurations and proposed various equations for SCFs at the crown, saddle, heel, and toe. Hosseini et al. [22] also investigated SCF in T/Y-joints subjected to IPB and OPB, and developed empirical models for SCF estimation at the crown (for IPB) and saddle (for OPB). Mohamed et al. [23] employed the ZPSS approach for CFRP-reinforced T/Y-joints subjected to either IPB or OPB moments and proposed equations for the toe under IPB and the saddle under OPB. More recently, Reshoe et al. [24] studied T/Y-joints under IPB, and proposed parametric models that incorporate material properties, such as the elastic modulus and thickness of the composite reinforcement and the steel joint, alongside geometric parameters. While all these studies focused on uniplanar bending loads, this paper advanced to explore the composite reinforcement of CHS KT-joints under multiplanar bending loads.

While all these studies focused on uniplanar bending loads, this paper advances the field by exploring the composite reinforcement of CHS KT-joints under multiplanar bending loads. Despite the significant progress in understanding SCFs in composite-reinforced CHS joints, there remains a lack of research on multiplanar bending conditions, which frequently occur in practical applications. Furthermore, the optimal reinforcement orientation for maximum SCF reduction has been sparsely investigated.

This study aims to address these gaps by developing empirical models to predict SCFs under multiplanar bending loads at 15-degree intervals around the joint interface. Additionally, it investigates the influence of reinforcement orientation on SCF reduction and validates the findings experimentally. The novelty of this work lies in its ability to provide a comprehensive framework for SCF estimation and its potential applications in enhancing the design and durability of CHS structures.

Table 2
Identification and range of critical parameters defining reinforced CHS KT-joint.

Parameters	Range	Reference / Logic
$\tau = t/T$	0.3–0.7	[54]
$\gamma = D/2T$	12–20	[54]
$\alpha = 2L/D$	5–40	[55,56]
$\beta = d/D$	0.4–0.8	[54]
$\zeta = g/D$	0.25–0.5	[57–59]
$\epsilon = E_{frp}/E_{steel}$	0–1.1	Derived based on E_{frp} and E_{steel}
$\eta = t_{frp}/T$	0–0.8	Derived based on t_{frp} and T
Inclined brace angle, Θ	30–75°	[54]
Gap between adjacent braces, g (mm)	100	[59]
Brace thickness (all), t (mm)	3–10	Manufacturing limit (assumption)
Chord thickness, T (mm)	3–10	Manufacturing limit (assumption)
Chord length, L (mm)	1800–3000	α_{max} , D_{max} , α_{min} , and D_{min}
Brace diameter, d (mm)	80–320	β_{max} , D_{min} , and D_{max}
Chord diameter, D (mm)	200–400	$D \geq 150$ [55], γ_{max} and T_{max}
Young's modulus of Steel, E_{steel} (GPa)	211	[60]
Young's modulus of FRP, E_{frp} (GPa)	0–230	Minimum: 0, Max: 230 GPa [61]
Thickness of FRP, t_{frp} (mm)	0–5	Min = unreinforced, Max = half of D_{max}

2. Methodology

This study utilises finite element analysis (FEA) using ANSYS Workbench to understand the stress field behaviour at the brace-chord interface of gapped KT-joints [35]. Several other studies have also employed FEA to explore the behaviour of CHS joints using ANSYS [12, 16, 19, 36–41] and ABAQUS [7–11, 14, 16, 18, 21, 22, 42–53], highlighting the broad applicability and acceptance of these tools for such research. Various KT-joint sizes were simulated, and the outcomes were employed to develop empirical models for rapid SCF estimation.

The FEA in this study was conducted with certain idealised assumptions. Residual stresses resulting from welding and fabrication processes were not incorporated into the model, as they might affect the stress distribution and SCFs. Additionally, the analysis assumed geometrically perfect welds, disregarding common imperfections such as undercuts or incomplete fusion, which could influence the results. The material properties and boundary conditions were also idealised, excluding potential variations due to environmental factors such as temperature fluctuations, moisture, or UV exposure. These

simplifications are necessary for computational feasibility, but may limit the direct applicability of the results to real-world conditions.

Relying solely on FEA for every joint may not be practical due to the required time, expertise, and computational resources. Therefore, these empirical models provide an efficient alternative for SCF estimation [15]. The behaviour of KT-joints was first analysed under both IPB and OPB individually, followed by the combination of these results to understand the response under multiplanar bending loads. A detailed breakdown of the methodology is provided in the following subsections.

2.1. Identification of critical parameters and their range

A typical KT-joint was modelled in ANSYS Workbench using the DesignModeler, where all geometric inputs were defined as parameters. The range of these inputs was established based on commonly used structural sizes and values referenced in the literature [25], considering typical joint configurations in practical applications and engineering guidelines. The selected ranges ensure that the model is applicable to a variety of configurations while accounting for practical material and manufacturing constraints. The geometric and composite reinforcement parameters were expressed in dimensionless form to cover a wide range of joint configurations, ensuring that the results remain applicable across different sizes and material types. The upper and lower bounds of these parameters were chosen to reflect typical engineering practices and material capabilities, as well as literature recommendations. A sensitivity analysis was performed to identify the critical parameters that influence SCF. Table 2 presents the identified parameters along with their respective ranges.

The parameters listed in Table 2 were selected based on a comprehensive review of the literature and practical considerations, such as manufacturing limits and material properties. For instance, the range of Young's modulus for FRP was chosen to encompass typical values observed in CFRP materials (0–230 GPa), with the lower bound representing an unreinforced joint ($E_{frp} = 0$), and the upper bound representing the maximum modulus found in high-performance CFRP. These parameter ranges allow for the assessment of a variety of real-world conditions, while the limitations on the maximum values reflect design constraints and material availability in current engineering practice. These choices ensure that the model can be applied to a broad range of composite-reinforced CHS KT-joints.

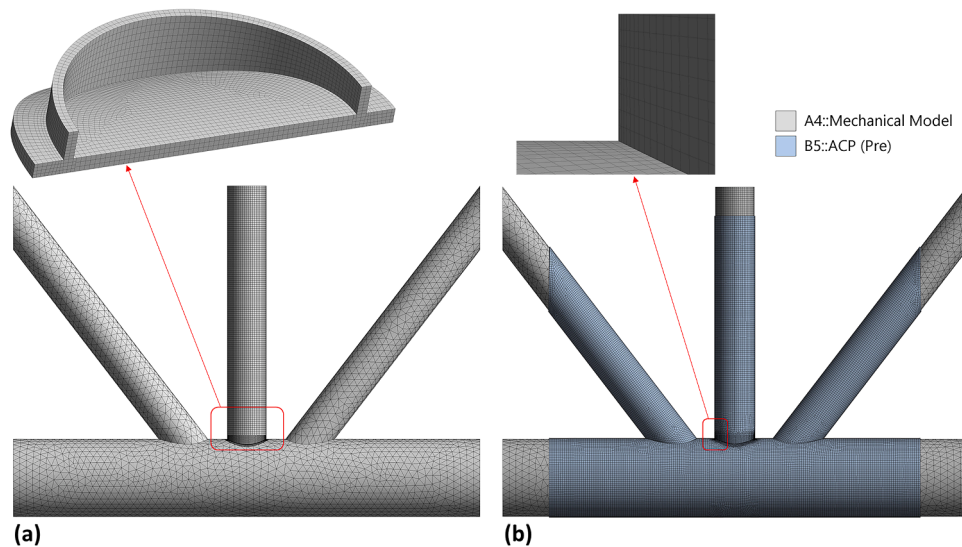


Fig. 1. Meshed model: (a) KT-joint (b) with reinforcement.

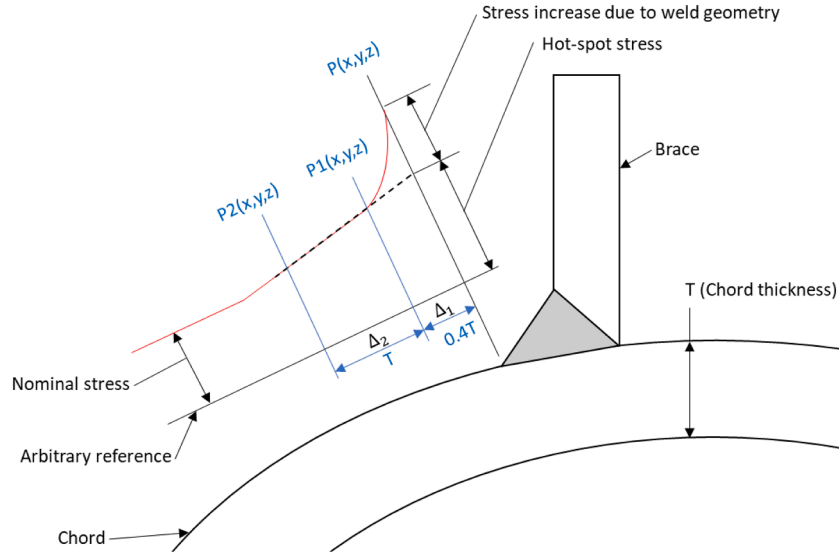


Fig. 2. Stress extrapolation at the weld toe [64].

2.2. Finite element modelling

The parametric geometry of the KT-joint was modelled using the DesignModeler of ANSYS Workbench to simulate the structural response under various types of bending loads. A MATLAB code was used to generate the required number of equidistant design points within the defined parameter range. The KT-joint was meshed using the Structural module of ANSYS Workbench. The meshed used high-order solid elements to ensure accurate stress distribution in the simulations. ANSYS automatically assigns the appropriate element type based on geometry and meshing criteria. The choice of higher-order elements ensures reliable stress distribution predictions, which is critical for determining accurate SCFs.

The joint volume was partitioned into various zones, and a relatively fine mesh was used at the critical regions. Various parametric sizing controls were applied to generate an acceptable mesh. Mesh independence was assessed by comparing the maximum percentage difference in SCF. If the difference in SCF was below 5 %, the number of elements was progressively reduced. This process was repeated until the error exceeded 5 %. These sizing controls created various numbers of elements for different design configurations of KT-joint within the defined geometric range. A typical KT-joint, sized according to the joint in Ahmadi et al. [62], was meshed using these finalised controls, resulting in 223,630 elements, as shown in Fig. 1. The applied composite reinforcement was meshed separately, comprising 76,234 elements. IPB and OPB were applied on the central brace of the joint and fixed from the chord ends.

Loads were incrementally increased during the simulation to ensure numerical stability.

The stress behaviour at the weld toe, as depicted in Fig. 2, can be significantly magnified due to the combined effect of geometry and weld notches. Since the weld notch effect is included in the S-N curves, it needs to be excluded through extrapolation of the stress on the weld toe, as recommended by Niemi et al. [63]. Specifically, the stresses at $0.4T$ and $1.4T$ (where T is the chord thickness) were linearly extrapolated to compute the HSS. The calculation was performed using Eqs. (2)–(4) [21, 48]. The stress magnitudes at reference points 1 and 2 (σ_1 and σ_2) are essential for determining the HSS. The positions of the weld notch and reference points are specified in global coordinates.

$$HSS = \sigma_1 + \left(\frac{\sigma_1 - \sigma_2}{\Delta_2} \right) \Delta_1 \quad (2)$$

$$\Delta_1 = \sqrt{(x_1 - x)^2 + (y_1 - y)^2 + (z - z_1)^2} \quad (3)$$

$$\Delta_2 = \sqrt{(x_2 - x_1)^2 + (y_2 - y_1)^2 + (z_2 - z_1)^2} \quad (4)$$

where

σ_1 = principal stress at reference point 1

σ_2 = principal stress at reference point 2

Δ_1 = distance between weld toe and reference point 1

Δ_2 = distance between reference point 1 and reference point 2

(x, y, z) = position coordinates of weld toe

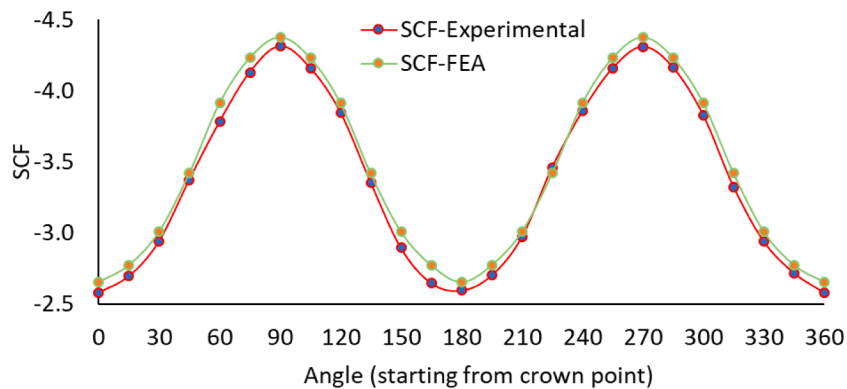


Fig. 3. Experimental validation of the FE model: (a) geometry (b) SCF comparison.

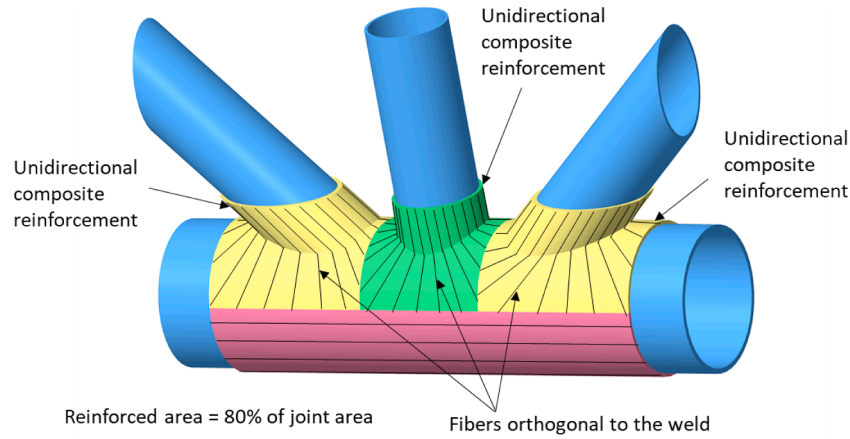


Fig. 4. Schematic of CFRP reinforcement of CHS KT-joint.

Table 3

Composite materials used for simulations [8,61,66].

Mechanical properties	Carbon/ epoxy (T300–5208)	Carbon/ epoxy (AS/3501)	Carbon/Epoxy-T700–12K
E_1 (GPa)	132	138	230
E_2 (GPa)	10.8	8.96	40
ν_{12}	0.24	0.3	0.27
G_{12} (GPa)	5.7	7.1	14.3
G_{13} (GPa)	5.7	7.1	14.3
G_{23} (GPa)	3.4	2.82	14.3

(x_1, y_1, z_1) = position coordinates of reference point 1

(x_2, y_2, z_2) = position coordinates of reference point 2

The finite element model was validated through static testing. Fig. 3 presents the comparison of SCF. The difference in numerical and experimental SCF values was below 8.6 %, validating the FE model. Once validated, the numerical model was reinforced with CFRP (carbon fibre-reinforced polymer composite). The optimal reinforcement strategy involves wrapping unidirectional composites with fibres oriented orthogonally to the weld toe [65]. The green-coloured area in Fig. 4 represents the composite wrapping around the central brace-chord interface, while the yellow-coloured area indicates the reinforcement applied to the inclined brace-chord interface. The lines illustrate the fibre directions in the composite reinforcement. Since SCF is a local phenomenon, it is primarily affected by the reinforcement at the interface, as represented in yellow in Fig. 4. Although the SCF was mainly reduced by reinforcing the interface area, for simplicity, 80 % of the joint area was reinforced. This decision was made to ensure that the interface region is fully covered with reinforcement, preventing any issues during finite element model generation. This approach also avoids the risk of incomplete or unsuccessful mesh generation, which could compromise the accuracy of the simulations. The joint was reinforced with CFRP, where the elastic modulus and thickness of composite reinforcement were defined as variables. Fig. 4 illustrates the reinforcement schematic.

Given that the mechanical response of composite materials primarily depends on the properties of the fibres, epoxy, and fabrication process; several CFRPs were used in the simulations. It was found that the primary difference lies in the elastic modulus along the fibre direction, while other properties exhibited minimal variation. The impact of these properties on SCF was analysed, and the reinforcement material properties, except for the elastic modulus (E_1), were fixed. The maximum E_1 value was selected for Carbon/Epoxy-T700–12 K [61], and simulations were conducted across the entire range of values, from zero to the maximum E_1 . Table 3 lists the properties of some CFRPs in this range. The elastic modulus along the fibre direction was defined as a ratio (ϵ) between the modulus of the composite material and the base joint

material for empirical modelling.

In addition to experimental validation, it was essential to ensure mesh-independent structural response across all design points. A variable was introduced to control the sizing parameters of the mesh used in the experimentally validated model, and the mesh was optimized through a convergence study. This study was conducted for joints with lower, middle, and upper dimension ranges, as shown in the three rows of Fig. 5. It was observed that while a coarser mesh was sufficient for larger joints, a finer mesh was required for smaller dimensions. The mesh convergence study demonstrated that the factor of 0.8 provided an optimal balance between mesh quality and computational efficiency. This factor was applied uniformly across all sections, ensuring that the mesh density across the joint and CFRP reinforcement was consistent and appropriate for accurate results. Various size controls were defined for different sections of the joint, and altering the mesh control factor affected the mesh density across all regions. A common mesh control factor of 0.8 was chosen for all subsequent simulations. This factor ensures mesh-independent results in the entire range for all the planar load configurations, as shown in Fig. 5.

The boundary conditions for the chord ends vary between pinned and fixed [67]. Both ends of the chord and inclined braces were fixed and load was applied to the central brace, as shown in Fig. 6. Static Structural simulation was conducted in the linear elastic range of material [68,69]. For steel, a linear elastic model was employed [60]. For CFRP, the material was modelled as a linear elastic orthotropic material with variable Young's modulus based on the range of properties derived from the literature and earlier simulations [8,61,66]. The choice of a linear elastic simulation was justified based on the assumption that the applied loads are within the elastic limit of both materials. While nonlinear effects, such as plasticity in steel and progressive failure in CFRP, could influence the response under extreme loading conditions, the structural HSS approach determines the fatigue strength entirely based on elastic behaviour. Material non-linearity and crack propagation are important but beyond the scope of this approach and this study. Since SCF is independent of the load magnitude when the stress in the joint is within the elastic limit [25]; any load within the elastic range could be used [70]. The applied IPB and OPB loads are defined by Eq. (5) [71].

$$\sigma_b = 32dM/[d^4 - (d - 2t)^4] \quad (5)$$

where

d = brace diameter

M = bending moment

t = brace thickness

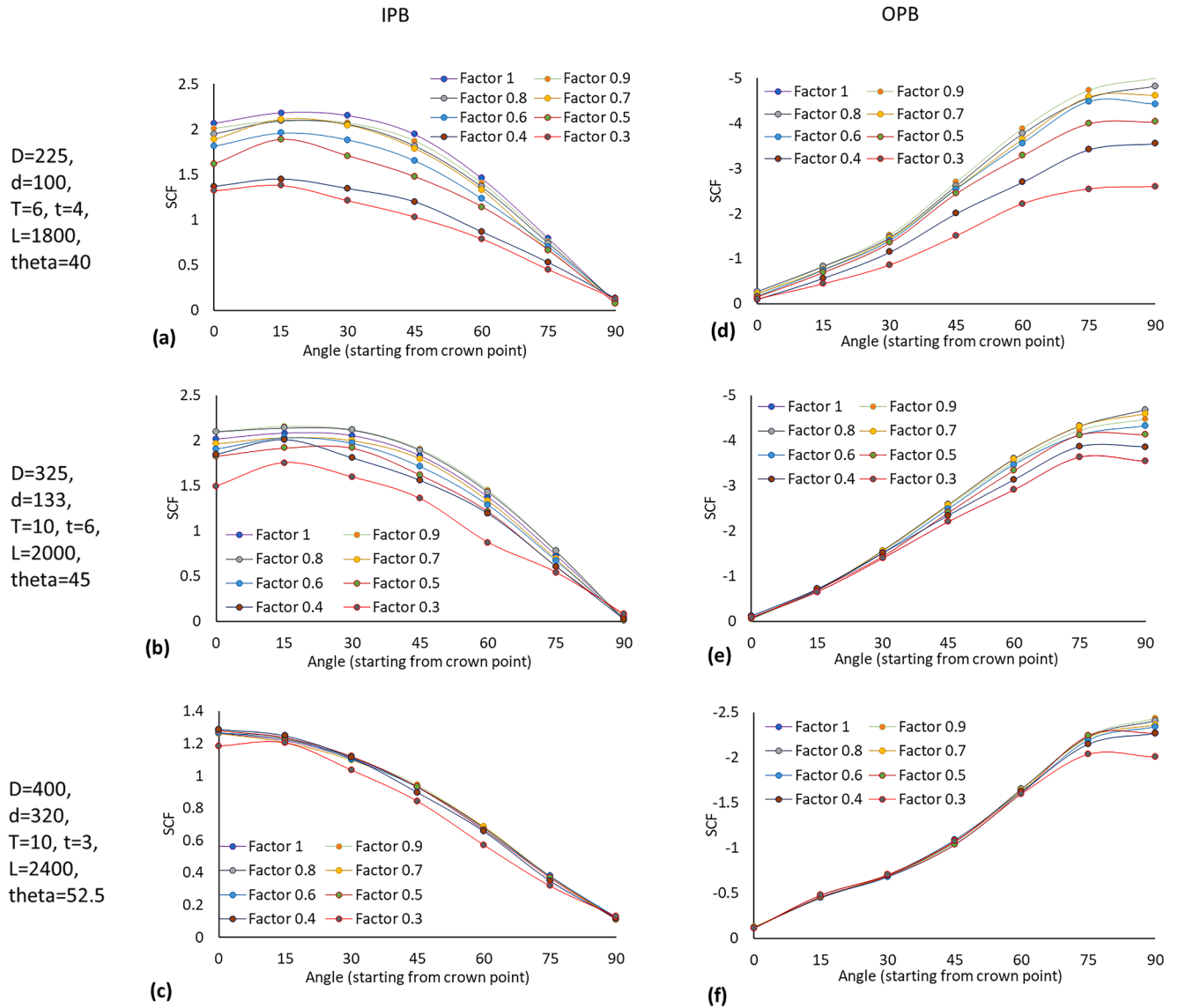


Fig. 5. Mesh sensitivity: IPB: (a), (b) and (c); OPB: (d), (e) and (f).

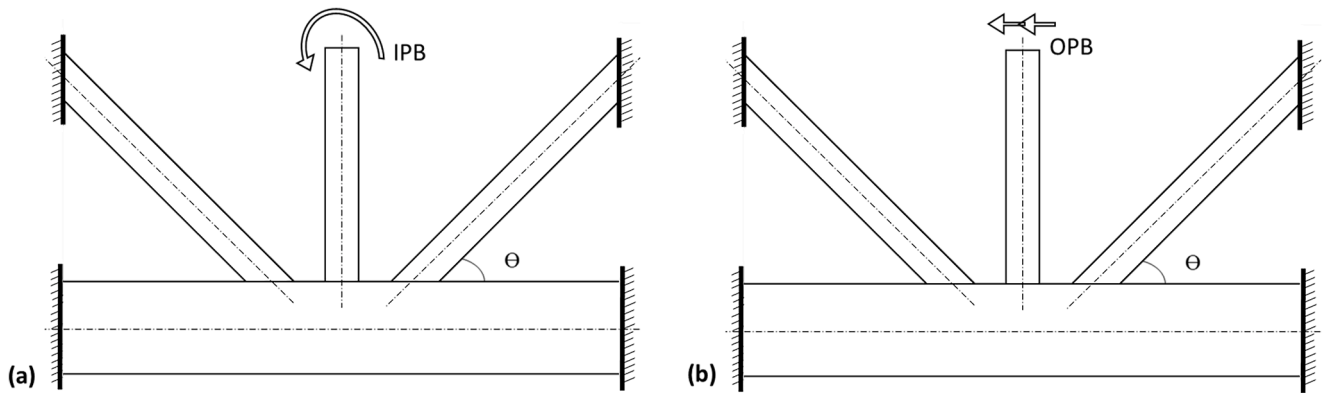


Fig. 6. Boundary conditions: (a) IPB (b) OPB.

2.3. ANN and empirical modelling

The results obtained from simulations of various KT-joint design configurations under IPB and OPB were used to train artificial neural

networks (ANN) [72]. Dimensionless parameters representing the joint geometry and CFRP reinforcement were defined as inputs, while the SCF at the interface was set as the output. A single hidden layer with 10 neurons was employed, as shown in Fig. 7. The network architecture

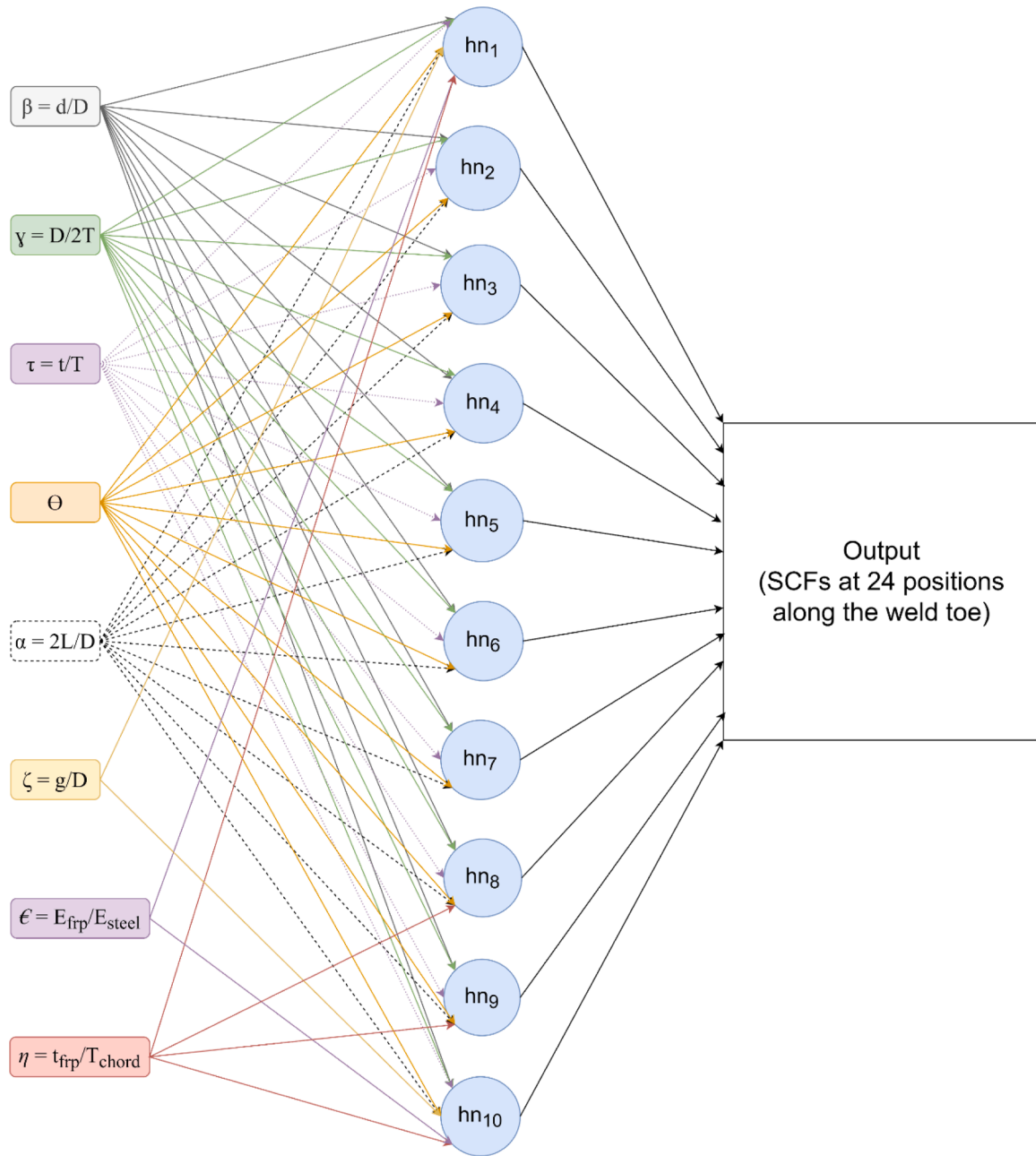


Fig. 7. Architecture of the ANN.

included input, hidden, and output layers, with the tan-sigmoid activation function applied to the hidden layer, and a linear activation function used for the output layer. The tan-sigmoid function is commonly used in neural networks to introduce nonlinearity, helping the model learn complex patterns, while the linear activation in the output layer allows for the prediction of continuous values. This combination has been widely employed in engineering applications for tasks such as regression and prediction due to its simplicity and effectiveness in capturing both nonlinear and linear relationships within the data. The choice of these activation functions aligns with typical practices in ANN modelling for structural and material properties prediction.

The ANN was trained using the Levenberg-Marquardt back-propagation algorithm. The Levenberg-Marquardt algorithm was selected for training due to its efficiency in handling large datasets while providing fast convergence, which is essential when working with complex, nonlinear problems. This algorithm combines the benefits of

both the Gauss-Newton method and gradient descent, making it suitable for ensuring robust and accurate predictions. The training process involved validation using a separate dataset to prevent overfitting, while cross-validation techniques were employed to enhance the generalization capability of the model. Training continued until the mean squared error (MSE) was less than 0.01 and the coefficient of performance exceeded 0.99 [29]. The trained network was exported to MATLAB as a function for further use. Additionally, the weights and biases from the best epoch were used to develop empirical equations to estimate the SCF in KT-joints under various configurations of bending loads.

2.4. Experimental validation

The developed empirical models were validated under IPB, OPB, and simultaneous application of both load components. A simplified test rig was designed for this purpose, incorporating a cable-pulley arrangement

for load application, as shown in Fig. 9. Dead weights were attached to the cable to apply the precalculated load in the desired direction. For the uniplanar and biplanar load cases, loads were applied incrementally using a cable-pulley arrangement to ensure precise control over the applied forces. In the uniplanar loading case, only one loading direction (either IPB or OPB) was applied. In the biplanar case, both IPB and OPB were applied separately in a controlled manner to simulate real-world conditions. For the multiplanar loading case, both IPB and OPB were applied simultaneously in their respective directions. In all cases, the load was increased gradually to prevent sudden stress changes and ensure stability.

SCFs were recorded using 48 strain gauges affixed to the chord near the weld toe. These gauges were installed at 24 stations along the weld toe, and the recorded strains were used to determine the HSS through linear extrapolation. SCF, the ratio of HSS to the nominal stress, is expressed in Eq. (1). Precise positioning of the joint was ensured to avoid any residual stress during the bolting process. Potential sources of error, including measurement inaccuracies, misalignment of the load cable, and the time required for strain gauges to stabilize, were carefully addressed to ensure accurate and reliable data acquisition. The geometric details of the tested joint are illustrated in Fig. 8, and the test setup used for the experimental validation is shown in the same figure. A cable-and-pulley arrangement was used for load application.

$$SCF = \frac{HSS}{\sigma_{nominal}} \quad (1)$$

3. Results and discussion

The peak HSS was observed around the crown for IPB and around the saddle point for OPB, consistent with the results of Ahmadi et al. [73]. However, under simultaneous IPB and OPB loading, the location of the

peak HSS shifted between the crown and saddle points, depending on the relative magnitudes of the applied loads. A typical KT-joint was modelled based on the geometric dimensions provided by Ahmadi et al. [62] and simulated under various configurations of bending loads to elaborate on these findings. When IPB and OPB were applied simultaneously, the location of the peak HSS shifted, as shown in Fig. 10.

Five typical IPB-to-OPB load ratios were simulated—4:1, 2:1, 1:1, 1:2, and 1:4—to examine the effect of the relative magnitudes of the load components. In these ratios, "1" represents a nominal load of 30 MPa. With an IPB of 30 MPa and OPB values of 30, 60, and 120 MPa, the peak HSS occurred at 15° for the first two cases and shifted to the saddle location in the third case. The percentage difference between the peak HSS and the HSS at the saddle or crown was insignificant in these scenarios. However, when an OPB of 30 MPa was combined with IPB loads of 30, 60, and 120 MPa, the peak HSS occurred at 15°, 30°, and 45° from the saddle point (between the crown and saddle). In these cases, the percentage differences in peak HSS from the HSS at the crown or saddle position were 10 %, 37 %, and 24 %, respectively, indicating significant variation. Thus, it can be concluded that the position of peak HSS is influenced by the relative magnitudes of IPB and OPB.

A total of 5429 designs were simulated for both IPB and OPB load cases. The simulation data was used to train ANNs, with the details summarised in Table 4. The generated data were used to train an ANN, achieving a COP of 0.9993 and 0.99939, and an MSE of 0.000319 and 0.0015 for IPB and OPB, respectively. The weights and biases of the best epoch from the trained ANN were used to develop empirical equations for rapid estimation of SCF in composite reinforced KT-joints subjected to IPB, as given by Eqs. (6) and (7). Similarly, the trained ANN was used to develop equations for SCF in KT-joints under OPB, as given by Eqs. (8) and (9).

$$\begin{bmatrix} h_1 \\ h_2 \\ h_3 \\ h_4 \\ h_5 \\ h_6 \\ h_7 \\ h_8 \\ h_9 \\ h_{10} \end{bmatrix} = \begin{bmatrix} -0.15 & 0.12 & -0.22 & 0.02 & 0.01 & -0.16 & 0.23 & 0.43 \\ 0.03 & -0.01 & -0.16 & 0.01 & 0.01 & 0.10 & -0.31 & 1.51 \\ 2.69 & 0.86 & 0.01 & -0.11 & 0.03 & -1.00 & 0.08 & 0.10 \\ 0.16 & -1.04 & -0.86 & 0.02 & -0.23 & 1.21 & -0.02 & 0.03 \\ -0.04 & 0.03 & -0.03 & -0.01 & 0.02 & -0.03 & -0.46 & -0.60 \\ -2.76 & -0.80 & 0.00 & 0.11 & -0.03 & 1.26 & -0.08 & -0.10 \\ 0.19 & 0.06 & 0.20 & 0.06 & 0.01 & -0.03 & -0.68 & -0.70 \\ 0.22 & -23.45 & -9.46 & 0.03 & -0.11 & 12.14 & -0.01 & -0.01 \\ -0.02 & 0.02 & -0.08 & -0.01 & 0.01 & -0.02 & -0.39 & -0.53 \\ 0.04 & -0.01 & -0.19 & 0.00 & 0.01 & 0.14 & 1.84 & -0.55 \end{bmatrix} \begin{bmatrix} \beta_n \\ \gamma_n \\ \tau_n \\ \theta_n \\ \alpha_n \\ \zeta_n \\ \epsilon \\ \eta \end{bmatrix} + \begin{bmatrix} -0.12 \\ 4.76 \\ -2.12 \\ 2.07 \\ -0.80 \\ 2.30 \\ -0.61 \\ -3.12 \\ -0.86 \\ 4.78 \end{bmatrix} \quad (6)$$

$$\begin{bmatrix} SCF_0 \\ SCF_{15} \\ SCF_{30} \\ SCF_{45} \\ SCF_{60} \\ SCF_{75} \\ SCF_{90} \end{bmatrix} = \begin{bmatrix} -0.42 & -71.94 & -20.88 & -0.15 & 3.45 & -20.76 & 0.40 & -0.09 & -4.80 & -31.85 \\ -0.50 & -63.02 & -19.74 & -0.14 & 3.64 & -19.61 & 0.22 & -0.09 & -4.83 & -31.49 \\ -0.53 & -56.19 & -9.86 & -0.14 & 3.75 & -9.77 & 0.11 & -0.09 & -4.83 & -29.37 \\ -0.55 & -53.98 & -2.02 & -0.15 & 3.92 & -1.98 & 0.05 & -0.10 & -4.95 & -28.61 \\ -0.53 & -50.69 & 8.87 & -0.17 & 4.03 & 8.86 & 0.01 & -0.10 & -5.02 & -26.94 \\ -0.50 & -39.88 & 29.62 & -0.23 & 3.48 & 29.51 & 0.01 & -0.08 & -4.36 & -21.91 \end{bmatrix} \begin{bmatrix} h_1 \\ h_2 \\ h_3 \\ h_4 \\ h_5 \\ h_6 \\ h_7 \\ h_8 \\ h_9 \\ h_{10} \end{bmatrix} + \begin{bmatrix} 102.41 \\ 93.13 \\ 84.19 \\ 81.24 \\ 76.31 \\ 60.68 \end{bmatrix} \quad (7)$$

$$\begin{bmatrix} h_1 \\ h_2 \\ h_3 \\ h_4 \\ h_5 \\ h_6 \\ h_7 \\ h_8 \\ h_9 \\ h_{10} \end{bmatrix} = \begin{bmatrix} 0.69 & -0.42 & 0.40 & 0.04 & 0.02 & -2.40 & 0.03 & 0.03 \\ 0.92 & 0.01 & 0.60 & -0.01 & 0.01 & -1.13 & 0.03 & 0.03 \\ 0.01 & -0.03 & -0.19 & 0.02 & 0.00 & 0.10 & 2.06 & -0.52 \\ 0.00 & 0.01 & 0.03 & 0.00 & 0.00 & 0.01 & -0.35 & -0.41 \\ -1.25 & 3.27 & 0.69 & 0.00 & 0.02 & 11.52 & -0.03 & -0.05 \\ 0.00 & -0.02 & -0.04 & 0.00 & 0.00 & -0.01 & 0.35 & 0.41 \\ 2.70 & -3.77 & 0.26 & -0.91 & 0.08 & -13.86 & 0.00 & 0.02 \\ 1.36 & 3.12 & -1.08 & -0.03 & 0.00 & 5.76 & 0.04 & 0.07 \\ -9.90 & -11.90 & -0.87 & 0.18 & -0.08 & -10.89 & -0.31 & -0.45 \\ -0.02 & 0.04 & 0.15 & -0.02 & -0.01 & -0.03 & 0.31 & -1.00 \end{bmatrix} \begin{bmatrix} \beta_n \\ \gamma_n \\ \tau_n \\ \theta_n \\ \alpha_n \\ \zeta_n \\ \epsilon \\ \eta \end{bmatrix} + \begin{bmatrix} -2.23 \\ -1.39 \\ 5.55 \\ -0.83 \\ 7.24 \\ 0.82 \\ -11.14 \\ 0.60 \\ -15.80 \\ -4.76 \end{bmatrix} \quad (8)$$

$$\begin{bmatrix} SCF_0 \\ SCF_{15} \\ SCF_{30} \\ SCF_{45} \\ SCF_{60} \\ SCF_{75} \\ SCF_{90} \end{bmatrix} = \begin{bmatrix} -1.92 & 1.02 & 85.59 & 71.68 & -0.35 & 70.46 & 0.10 & 0.10 & 0.12 & -175.75 \\ -1.20 & 0.70 & 132.23 & 109.42 & -0.17 & 107.56 & 0.14 & -0.03 & -0.02 & -282.25 \\ -0.83 & 0.76 & 110.60 & 108.74 & -0.28 & 106.80 & -0.08 & 0.17 & 0.15 & -259.53 \\ -0.88 & 0.98 & 108.22 & 107.16 & -0.42 & 105.23 & -0.27 & 0.35 & 0.32 & -257.99 \\ -0.98 & 1.14 & 107.98 & 106.62 & -0.50 & 104.71 & -0.38 & 0.45 & 0.42 & -257.99 \\ -0.99 & 1.15 & 108.19 & 104.96 & -0.50 & 103.09 & -0.39 & 0.46 & 0.43 & -254.75 \end{bmatrix} \begin{bmatrix} h_1 \\ h_2 \\ h_3 \\ h_4 \\ h_5 \\ h_6 \\ h_7 \\ h_8 \\ h_9 \\ h_{10} \end{bmatrix} + \begin{bmatrix} -259.73 \\ -412.09 \\ -367.28 \\ -363.17 \\ -362.85 \\ -359.85 \end{bmatrix} \quad (9)$$

The empirical models developed for SCF estimation under uniplanar loads can be extended to estimate the combined HSS for composite-reinforced KT-joints subjected to multiplanar loads. By superimposing the HSS values obtained from uniplanar loads at the 24 positions along the weld toe, the combined HSS can be estimated. This combined HSS is used to identify the peak HSS, which allows for the estimation of fatigue life when used with the S-N curve.

The recorded strains for IPB are shown in Fig. 11. These strains were converted into SCFs, as presented in Fig. 12. The difference between the experimental and predicted SCFs in the region of maximum SCF was less than 10 %, which is within acceptable limits.

The same KT-joint was then subjected to OPB, and the strain

response was recorded. The measured strains and the corresponding SCFs are presented in Fig. 13 and Fig. 14, respectively. The results indicate a close match between the experimental SCF and the FEA-based SCF. The maximum difference in the region of maximum SCF was less than 8.5 %, which is within the acceptable limit.

The fabricated joint was experimentally tested under multiplanar bending loads, i.e., loads with components in both the IPB and OPB directions. Following the same methodology used for the previous load cases, strains were recorded and used to determine the HSS at 24 positions along the weld toe of the chord-central brace interface in the KT-joint. The recorded strains are presented in Fig. 15, and the corresponding HSS values are shown in Fig. 16. Three configurations of IPB

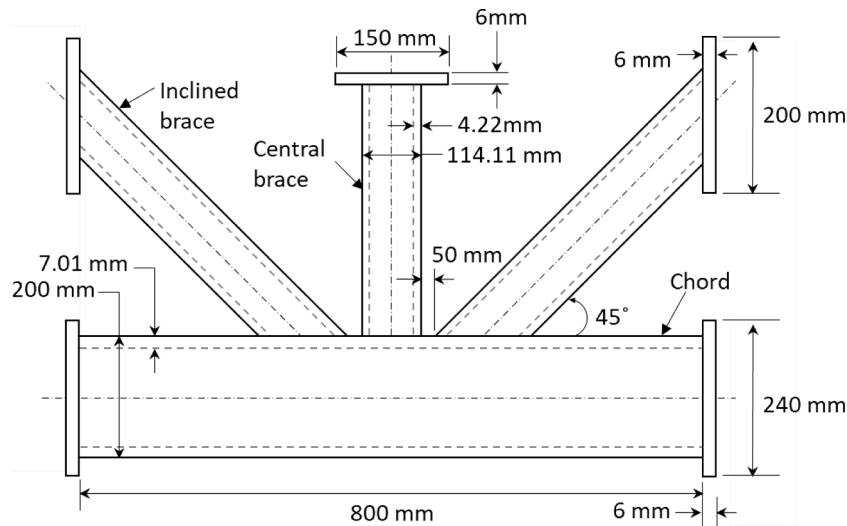


Fig. 8. Dimensions of the KT-joint used for experimental validation.

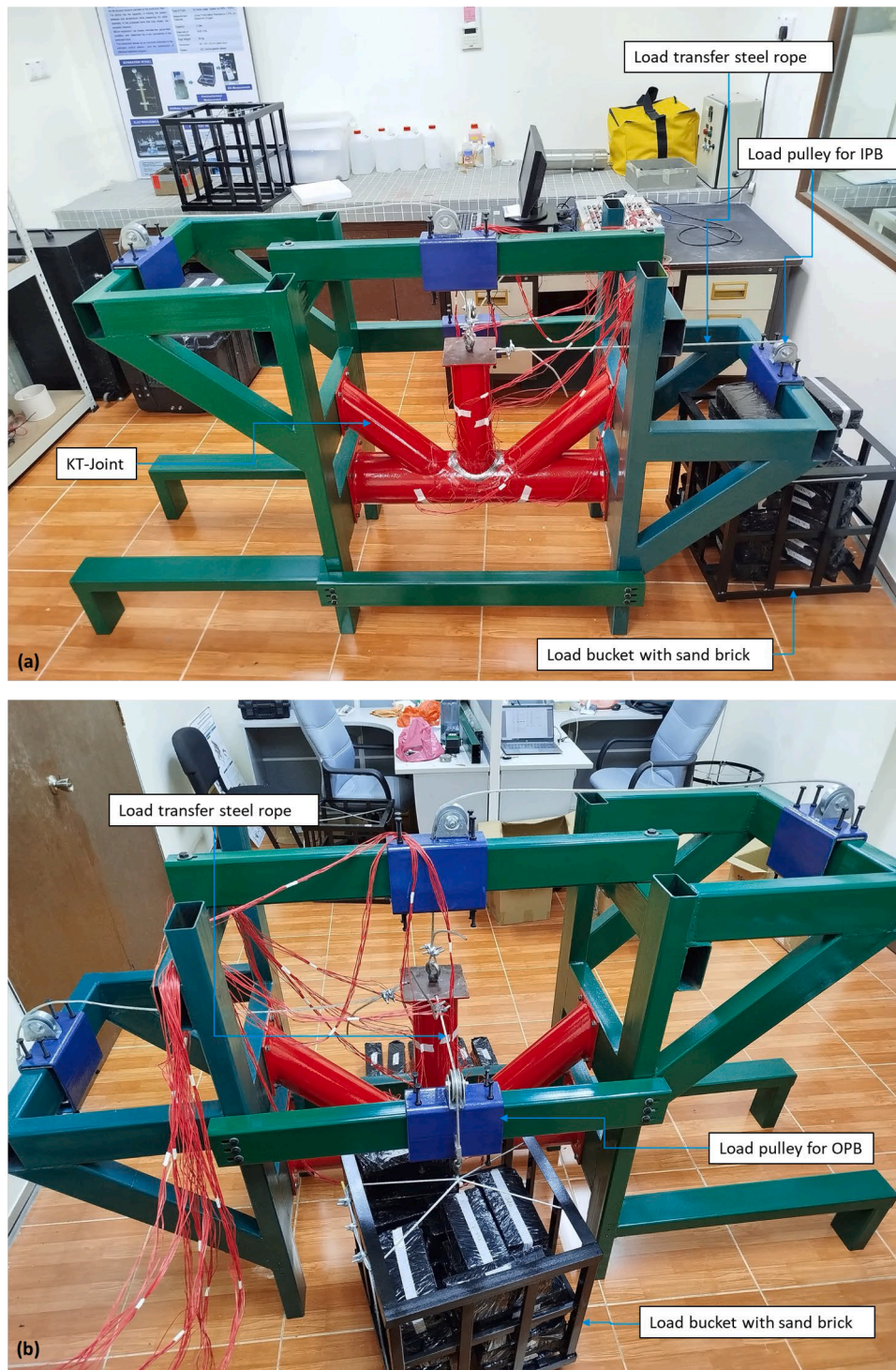


Fig. 9. Setup for testing KT-joint: (a) IPB (b) OPB.

were tested: 1:1, 1:2, and 2:1. The combined effect of IPB and OPB loads was considered in this study. The interaction between these loading types was investigated through the principle of superposition, which assumes that the total stress response is the sum of the individual stress responses caused by each loading type. IPB and OPB loads can have significant interactions, with the location of maximum SCF being influenced by the direction and magnitude of the applied loads. The superposition of these bending loads can lead to non-intuitive stress distributions, potentially shifting the location of peak SCFs and introducing stress concentrations in regions that would not be as critical

under single-axis loading.

Fig. 16 indicates that the position of maximum SCF depends on the relative magnitudes of IPB and OPB, necessitating models capable of estimating SCF at intermediate points between the crown and saddle. These visualizations show how the superposition of the bending moments influences the stress concentration areas, especially in regions where the maximum SCF occurs. The stress distribution and location of the maximum SCF are affected by the magnitude and direction of the applied loads. The maximum difference in the region of peak SCF was less than 15 %, falling within the acceptable threshold determined by

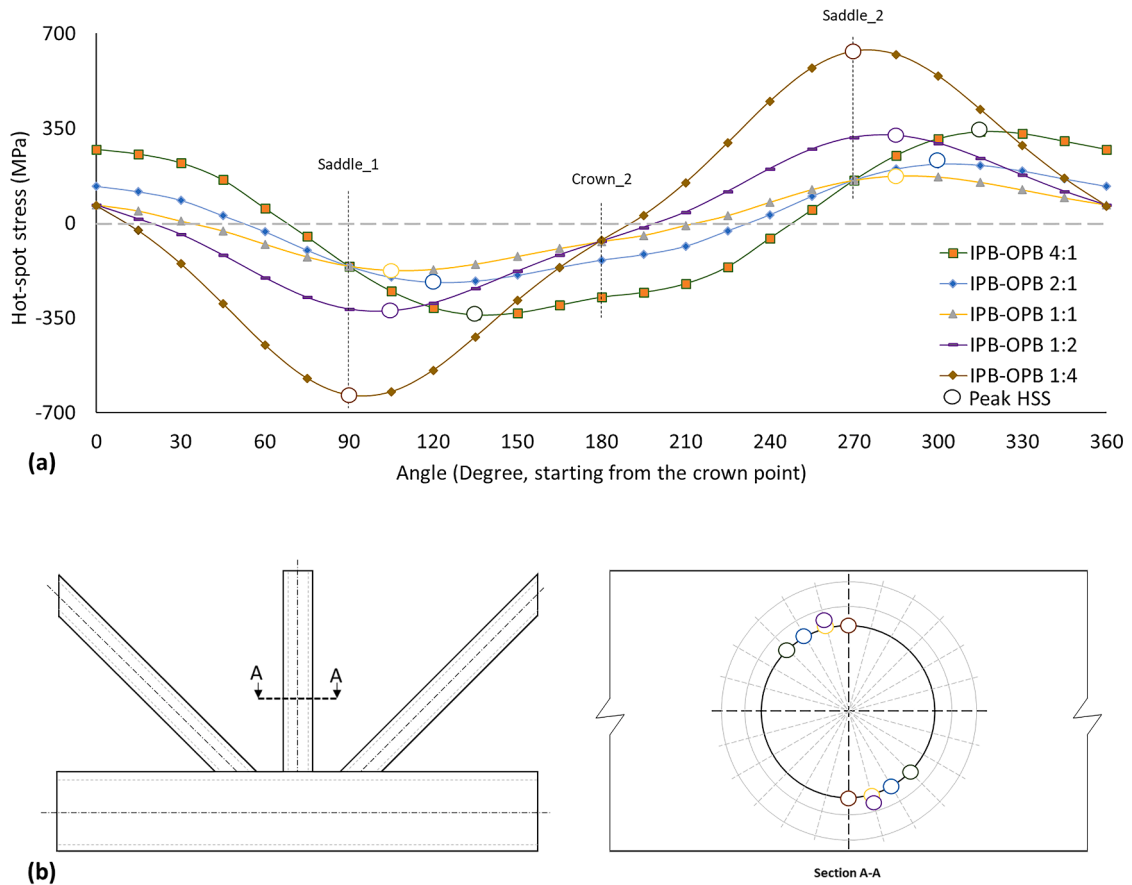


Fig. 10. KT-joint under bending loads: (a) HSS (b) position of peak HSS.

Table 4

Details of ANN used for empirical modelling.

S. No.	Load case	# of simulations	Coefficient of performance	Mean square error
1.	IPB	10858	0.994321	0.000271
2.	OPB	10858	0.99714	0.001455

the difference between experimental and numerical results reported by Ahmadi et al. [70].

The empirical models developed in this study are specifically designed for KT-joints subjected to bending loads applied to the central brace. These models are applicable under various uniplanar, bi-planar,

and multiplanar load configurations. However, it is important to note that these models are not directly transferable to other types of CHS joints, as different joint geometries and loading conditions would require separate modelling efforts. Each type of joint must have specific empirical models developed using the same methodology employed in this study, including finite element simulations and artificial neural networks. This approach highlights the need for future research to develop tailored models for other joint configurations, ensuring their accuracy and applicability.

4. Conclusion

This study analysed 10,858 CFRP-reinforced circular hollow section KT-joints under various bending load configurations. The magnitude of

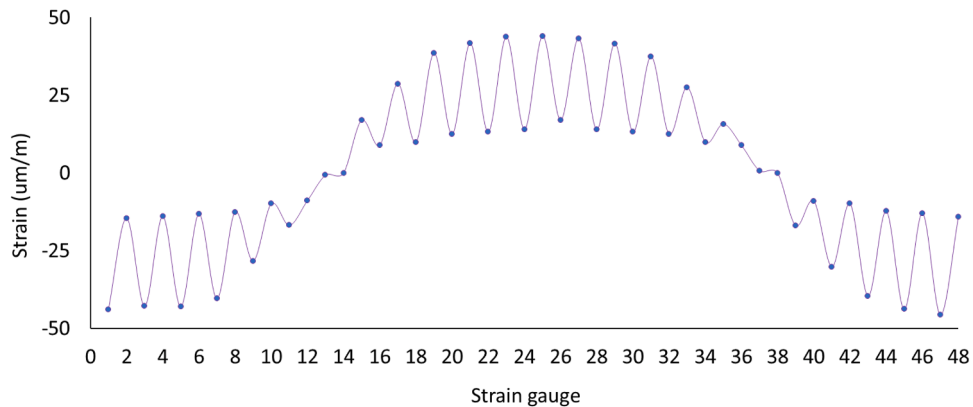


Fig. 11. Strains recorded in KT-joint subjected to IPB.

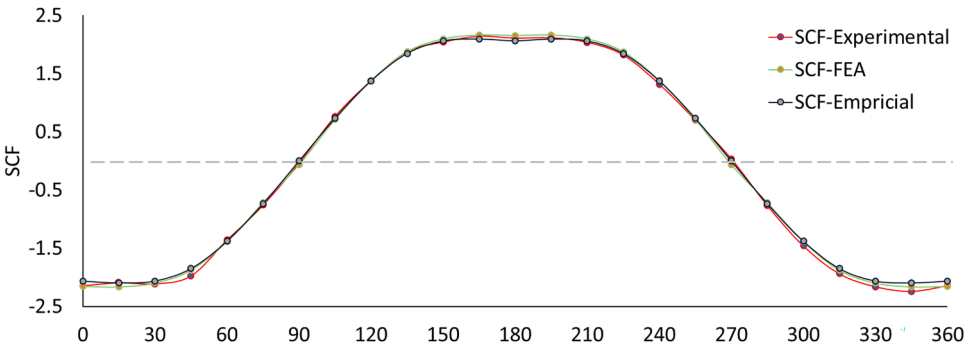


Fig. 12. SCFs in KT-joint subjected to IPB.

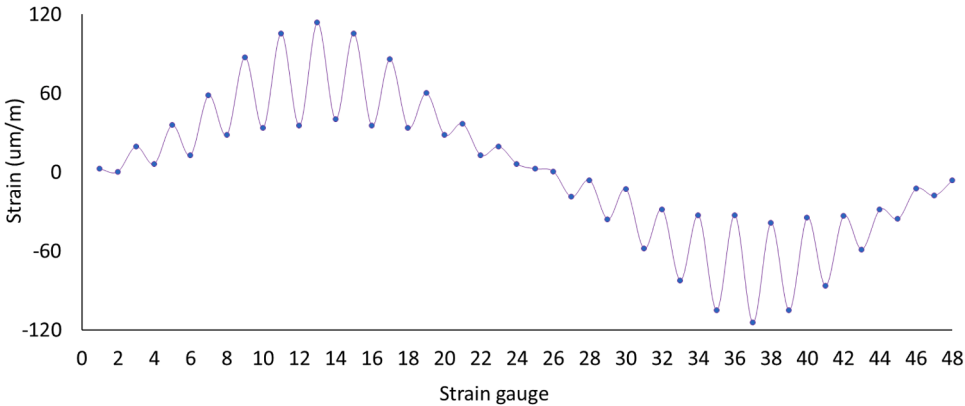


Fig. 13. Strains recorded in KT-joint subjected to OPB.

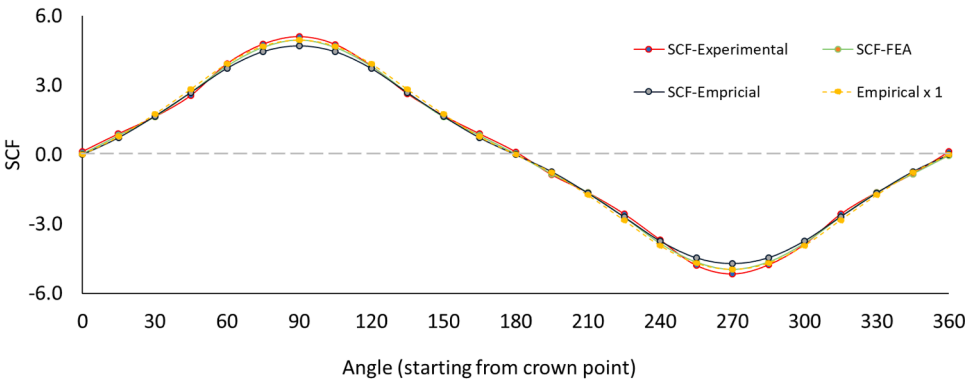


Fig. 14. SCFs in KT-joint subjected to OPB.

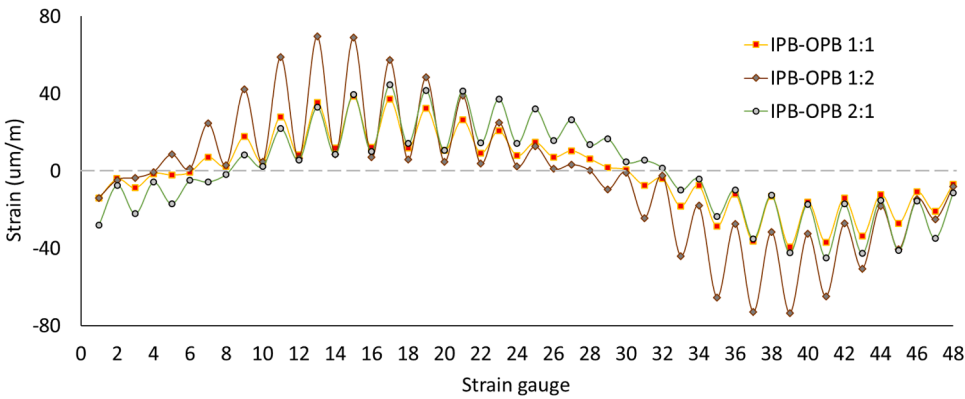


Fig. 15. Strain normal to the weld profile in KT-joint under IPB-OPB.

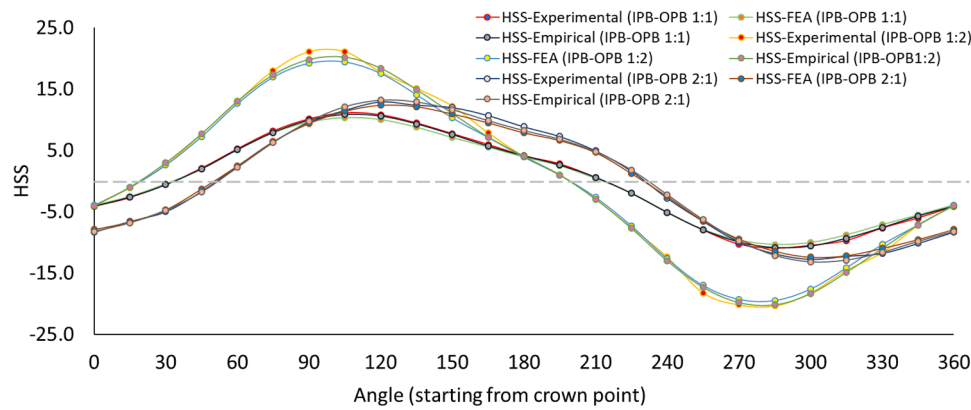


Fig. 16. Comparison of SCFs in KT-joint under IPB-OPB.

the Stress Concentration Factor (SCF) was primarily influenced by the thickness, orientation, and elastic modulus of the reinforcement. Artificial neural network models were trained using the simulation data, and empirical models were developed for determining SCF and hot-spot stress (HSS) in CFRP-reinforced KT-joints under uniplanar and multi-planar bending loads at 24 positions along the weld toe at the chord-brace interface. The novel empirical models accurately predict the peak HSS, enabling realistic estimation of fatigue life using the respective S-N curves. These models were experimentally validated, with a maximum error of less than 15 % at the location of peak HSS, which is within the acceptable range. This study provides valuable insights into the impact of CFRP reinforcement on stress concentration factors under complex loading scenarios, contributing to enhanced structural design and optimisation strategies. Future research can address the assumptions made in this study, such as the exclusion of residual stresses and weld imperfections, and explore their influence on SCFs and hot-spot stress predictions. Additionally, investigating the effects of environmental factors such as temperature or moisture variations and alternative reinforcement materials could further enhance the applicability of these findings.

Funding

This research was funded by Yayasan Universiti Teknologi PETRONAS under Grant No. 015LC0-443.

Declaration of competing interest

The authors declare that they have no known competing financial interests or personal relationships that could have appeared to influence the work reported in this paper.

References

- [1] X.L. Zhao, L. Zhang, State-of-the-art review on FRP strengthened steel structures, *Eng. Struct.* 29 (2007) 1808–1823, <https://doi.org/10.1016/j.engstruct.2006.10.006>.
- [2] J.G. Teng, T. Yu, D. Fernando, Strengthening of steel structures with fiber-reinforced polymer composites, *J. Constr. Steel. Res.* 78 (2012) 131–143, <https://doi.org/10.1016/j.jcsr.2012.06.011>.
- [3] A.A. Kadry, A.M. Ebid, E.N. El-Ganzoury, S.Y. Aboul Haggag, A. Mokhtar A salam, Capacity of unstiffened multi-planar tubular KK-gap joints under anti-symmetric loading, *Resul. Eng* 18 (2023) 101092, <https://doi.org/10.1016/j.rineng.2023.101092>.
- [4] M. Iqbal, S. Karuppanan, V. Perumal, M. Ovinis, A. Rasul, Rehabilitation techniques for offshore tubular joints, *J. Mar. Sci. Eng.* 11 (2023) 461, <https://doi.org/10.3390/jmse11020461>.
- [5] C.P. Pantelides, J. Nadeau, L. Cercone, Repair of cracked aluminum overhead sign structures with glass fiber reinforced polymer composites, *J. Compos. Constr.* 7 (2003) 118–126, [https://doi.org/10.1061/\(asce\)1090-0268\(2003\)7:2\(118\)](https://doi.org/10.1061/(asce)1090-0268(2003)7:2(118)).
- [6] A. Fam, S. Witt, S. Rizkalla, Repair of damaged aluminum truss joints of highway overhead sign structures using FRP, *Constr. Build. Mater.* 20 (2006) 948–956, <https://doi.org/10.1016/j.conbuildmat.2005.06.014>.
- [7] C. Chen, Y. Shao, J. Yang, Study on static strength of circular hollow section (CHS) T-joint reinforced with FRP, *Appl. Mech. Mater.* 99–100 (2011) 72–75, <https://doi.org/10.4028/www.scientific.net/AMM.99-100.72>.
- [8] Y. Fu, L. Tong, L. He, X.L. Zhao, Experimental and numerical investigation on behavior of CFRP-strengthened circular hollow section gap K-joints, *Thin-Walled Struct.* 102 (2016) 80–97, <https://doi.org/10.1016/j.tws.2016.01.020>.
- [9] M. Lesani, M.R. Bahaari, M.M. Shokrieh, Numerical investigation of FRP-strengthened tubular T-joints under axial compressive loads, *Compos. Struct.* 100 (2013) 71–78, <https://doi.org/10.1016/j.compstruct.2012.12.020>.
- [10] M. Lesani, M.R. Bahaari, M.M. Shokrieh, Numerical investigation of FRP-strengthened tubular T-joints under axial compressive loads, *Constr. Build. Mater.* 53 (2014) 243–252, <https://doi.org/10.1016/j.conbuildmat.2013.11.097>.
- [11] M. Lesani, M.R. Bahaari, M.M. Shokrieh, FRP wrapping for the rehabilitation of circular hollow section (CHS) tubular steel connections, *Thin-Walled. Struct.* 90 (2015) 216–234, <https://doi.org/10.1016/j.tws.2014.12.013>.
- [12] P.S. Prashob, A.P. Shashikala, T.P. Somasundaran, Behaviour of carbon fiber reinforced polymer strengthened tubular joints, *Steel. Compos. Struct.* 24 (2017) 383–390, <https://doi.org/10.12989/scs.2017.24.4.383>.
- [13] M. Alembagheri, M. Rashidi, A. Yazdi, B. Samali, Numerical analysis of axial cyclic behavior of FRP retrofitted CHS joints, *Materials (Basel)* 14 (2021) 1–14, <https://doi.org/10.3390/ma14030648>.
- [14] A. Yazdi, M. Rashidi, M. Alembagheri, B. Samali, Buckling behavior of non-retrofitted and frp-retrofitted steel CHS T-joints, *Appl. Sci* 11 (2021) 1–13, <https://doi.org/10.3390/app11073098>.
- [15] M. Iqbal, S. Karuppanan, V. Perumal, M. Ovinis, M. Iqbal, A systematic review of stress concentration factors (SCFs) in composite reinforced circular hollow section (CHS) joints, *Compos. Part C Open Access* 15 (2024) 100515, <https://doi.org/10.1016/j.jcomc.2024.100515>.
- [16] A. Sadat Hosseini, M.R. Bahaari, M. Lesani, Parametric study of FRP strengthening on stress concentration factors in an offshore tubular T-joint subjected to in-plane and out-of-plane bending moments, *Int. J. Steel. Struct.* 19 (2019) 1755–1766, <https://doi.org/10.1007/s13296-019-00244-0>.
- [17] H. Nassiraei, P. Rezaadoost, Stress concentration factors in tubular T/Y-connections reinforced with FRP under in-plane bending load, *Mar. Struct.* 76 (2021) 102871, <https://doi.org/10.1016/j.marstruc.2020.102871>.
- [18] H. Nassiraei, P. Rezaadoost, Parametric study and formula for SCFs of FRP-strengthened CHS T/Y-joints under out-of-plane bending load, *Ocean Eng* 221 (2021) 108313, <https://doi.org/10.1016/j.oceaneng.2020.108313>.
- [19] H. Nassiraei, P. Rezaadoost, SCFs in tubular X-joints retrofitted with FRP under out-of-plane bending moment, *Mar. Struct.* 79 (2021) 103010, <https://doi.org/10.1016/j.marstruc.2021.103010>.
- [20] H. Nassiraei, P. Rezaadoost, SCFs in tubular X-connections retrofitted with FRP under in-plane bending load, *Compos. Struct.* 274 (2021) 114314, <https://doi.org/10.1016/j.compstruct.2021.114314>.
- [21] E. Zavvar, A. Sadat Hosseini, M.A. Lotfollahi-Yaghin, Stress concentration factors in steel tubular KT-connections with FRP-Wrapping under bending moments, *Structures* 33 (2021) 4743–4765, <https://doi.org/10.1016/j.istruc.2021.06.100>.
- [22] A. Sadat Hosseini, M.R. Bahaari, M. Lesani, Formulas for stress concentration factors in T&Y steel tubular joints stiffened with FRP under bending moments, *Int. J. Steel. Struct.* 22 (2022) 1408–1432, <https://doi.org/10.1007/s13296-022-00651-w>.
- [23] H.S. Mohamed, X.S. Yang, F.Y. Liao, T. Fu, SCF determination of the CFRP- fortified T/Y-joints exposed to IPB or OPB moment via ZPSS approach, *Structures* 61 (2024), <https://doi.org/10.1016/j.istruc.2024.105997>.
- [24] R. Rashnooe, M. Zeinoddini, E. Ghafouri, M. Sharafi, Experimental and numerical study on the in-plane bending behaviour of FRP-strengthened steel tubular welded T-joints, *Thin-Walled. Struct.* 201 (2024) 112000, <https://doi.org/10.1016/j.tws.2024.112000>.
- [25] M. Iqbal, S. Karuppanan, V. Perumal, M. Ovinis, H. Nouman, Empirical modeling of stress concentration factors using finite element analysis and artificial neural networks for the fatigue design of tubular KT-joints under combined loading, *Fatigue. Fract. Eng. Mater. Struct.* 46 (2023) 4333–4349, <https://doi.org/10.1111/ffe.14122>.

- [26] K.H. Hoon, L.K. Wong, A.K. Soh, Experimental investigation of a doubler-plate reinforced tubular T-joint subjected to combined loadings, *J. Constr. Steel. Res* 57 (2001) 1015–1039, [https://doi.org/10.1016/S0143-974X\(01\)00023-2](https://doi.org/10.1016/S0143-974X(01)00023-2).
- [27] K.C. Gulati, W.J. Wang, D.K.Y. Kan, An analytical study of stress concentration effects in multibrace joints under combined loading, in: *Proc. Annu. Offshore Technol. Conf* 4407, USA: OTC, Houston, Texas, 1982, pp. 337–342, <https://doi.org/10.4043/4407-ms>, vol. 1982–May.
- [28] M. Iqbal, S. Karuppanan, V. Perumal, M. Faizan, A. Rasul, M. Iqbal, Modeling stress concentration factors for fatigue design of KT-joints subjected to in-plane bending loads using artificial neural networks, *Int. J. Eng. Res. Africa* 71 (2024) 79–92, <https://doi.org/10.4028/p-zOom9>.
- [29] M. Iqbal, S. Karuppanan, V. Perumal, M. Ovinis, A. Hina, An artificial neural network model for the stress concentration factors in KT-joints subjected to axial compressive load, *Mater. Sci. Forum* 1103 (2023) 163–175, <https://doi.org/10.4028/p-yo50i>.
- [30] A. Rasul, S. Karuppanan, V. Perumal, M. Ovinis, M. Iqbal, Ultimate strength of internal ring-reinforced KT joints under brace axial compression, *Civ. Eng. J* 10 (2024) 1543–1560, <https://doi.org/10.28991/CEJ-2024-010-05-012>.
- [31] A. Rasul, S. Karuppanan, V. Perumal, M. Ovinis, M. Iqbal, Multi-objective optimization of stress concentration factors for fatigue design of internal ring-reinforced KT-joints undergoing brace axial compression, *Civ. Eng. J* 10 (2024) 1742–1764, <https://doi.org/10.28991/CEJ-2024-010-06-03>.
- [32] A. Rasul, S. Karuppanan, V. Perumal, M. Ovinis, M. Iqbal, An artificial neural network model for determining stress concentration factors for fatigue design of tubular T-joint under compressive loads, *Int. J. Struct. Integr* 15 (2024) 633–652, <https://doi.org/10.1108/IJSI-02-2024-0034>.
- [33] A. Rasul, S. Karuppanan, V. Perumal, M. Ovinis, M. Iqbal, K. Alam, Empirical modeling of stress concentration factors using artificial neural networks for fatigue design of tubular T-joint under in-plane and out-of-plane bending moments, *Int. J. Struct. Integr* 15 (2024) 757–776, <https://doi.org/10.1108/IJSI-03-2024-0043>.
- [34] M. Iqbal, S. Karuppanan, V. Perumal, M. Ovinis, M. Iqbal, A. Rasul, Optimization of fibre orientation for composite reinforcement of circular hollow section KT-joints, *Int. J. Struct. Integr.* 15 (2024) 717–730, <https://doi.org/10.1108/IJSI-04-2024-0054>.
- [35] A.A. Kadry, A.M. Ebid, A. Mokhtar A salaam, E.N. El-Ganzoury, S.Y.A. Haggag, Parametric study of unstiffened multi-planar tubular KK-Joints, *Resul. Eng* 14 (2022) 100400, <https://doi.org/10.1016/j.rineng.2022.100400>.
- [36] P.S. Prashob, A.P. Shashikala, T.P. Somasundaran, Characteristics of CFRP strengthened tubular joints subjected to different monotonic loadings, *Steel. Compos. Struct.* 32 (2019) 361–372, <https://doi.org/10.12989/scs.2019.32.3.361>.
- [37] H. Nassiraei, P. Rezadoost, Stress concentration factors in tubular T/Y-joints strengthened with FRP subjected to compressive load in offshore structures, *Int. J. Fatigue* 140 (2020) 105719, <https://doi.org/10.1016/j.ijfatigue.2020.105719>.
- [38] H. Nassiraei, P. Rezadoost, Local joint flexibility of tubular T/Y-joints retrofitted with GFRP under in-plane bending moment, *Mar. Struct.* 77 (2021) 102936, <https://doi.org/10.1016/j.marstruc.2021.102936>.
- [39] H. Nassiraei, P. Rezadoost, Development of a probability distribution model for the SCFs in tubular X-connections retrofitted with FRP, *Structures* 36 (2022) 233–247, <https://doi.org/10.1016/j.istruc.2021.10.033>.
- [40] E. Zavvar, J. Henneberg, C. Guedes Soares, Stress concentration factors in FRP-reinforced tubular DKT joints under axial loads, *Mar. Struct.* 90 (2023) 429–452, <https://doi.org/10.1016/j.marstruc.2023.103429>.
- [41] P. Rezadoost, H. Nassiraei, Identification of the most suitable probability distributions for ultimate strength of FRP-strengthened X-shaped tubular joints under axial loads, *Ocean Eng* 290 (2023) 116292, <https://doi.org/10.1016/j.oceaneng.2023.116292>.
- [42] A. Sadat Hosseini, M.R. Bahaari, M. Lesani, Stress concentration factors in FRP-strengthened offshore steel tubular T-joints under various brace loadings, *Structures* 20 (2019) 779–793, <https://doi.org/10.1016/j.istruc.2019.07.004>.
- [43] L. Tong, G. Xu, X.L. Zhao, H. Zhou, F. Xu, Experimental and theoretical studies on reducing hot spot stress on CHS gap K-joints with CFRP strengthening, *Eng. Struct.* 201 (2019) 296–313, <https://doi.org/10.1016/j.engstruct.2019.109827>.
- [44] P. Deng, B. Yang, X. Chen, Y. Liu, Experimental and numerical investigations of the compressive behavior of carbon fiber-reinforced polymer-strengthened tubular steel T-joints, *Front. Struct. Civ. Eng.* 14 (2020) 1215–1231, <https://doi.org/10.1007/s11709-020-0663-y>.
- [45] G. Xu, L. Tong, X.L. Zhao, H. Zhou, F. Xu, Numerical analysis and formulae for SCF reduction coefficients of CFRP-strengthened CHS gap K-joints, *Eng. Struct.* 210 (2020) 369–386, <https://doi.org/10.1016/j.engstruct.2020.110369>.
- [46] A. Sadat Hosseini, M.R. Bahaari, M. Lesani, Experimental and parametric studies of SCFs in FRP strengthened tubular T-joints under axially loaded brace, *Eng. Struct.* 213 (2020) 110548, <https://doi.org/10.1016/j.engstruct.2020.110548>.
- [47] A.S. Hosseini, M.R. Bahaari, M. Lesani, SCF distribution in FRP-strengthened tubular T-joints under brace axial loading, *Sci. Iran* 27 (2020) 1113–1129, <https://doi.org/10.24200/SCI.2018.5471.1293>.
- [48] A. Sadat Hosseini, E. Zavvar, H. Ahmadi, Stress concentration factors in FRP-strengthened steel tubular KT-joints, *Appl. Ocean Res.* 108 (2021) 1187–1221, <https://doi.org/10.1016/j.apor.2021.102525>.
- [49] A. Sadat Hosseini, M.R. Bahaari, M. Lesani, P. Hajikarimi, Static load-bearing capacity formulation for steel tubular T/Y-joints strengthened with GFRP and CFRP, *Compos. Struct.* 268 (2021) 263–281, <https://doi.org/10.1016/j.compstruct.2021.113950>.
- [50] H.S. Mohamed, Y. Shao, C. Chen, M. Shi, Static strength of CFRP-strengthened tubular TT-joints containing initial local corrosion defect, *Ocean Eng.* 236 (2021) 109484, <https://doi.org/10.1016/j.oceaneng.2021.109484>.
- [51] X. Xu, Y. Shao, X. Gao, H.S. Mohamed, Stress concentration factor (SCF) of CHS gap TT-joints reinforced with CFRP, *Ocean Eng.* 247 (2022) 110722, <https://doi.org/10.1016/j.oceaneng.2022.110722>.
- [52] M. Lesani, A. Sadat Hosseini, M.R. Bahaari, Load bearing capacity of GFRP-strengthened tubular T-joints: experimental and numerical study, *Structures* 38 (2022) 1151–1164, <https://doi.org/10.1016/j.istruc.2022.01.092>.
- [53] H.S. Mohamed, L. Zhang, Y.B. Shao, X.S. Yang, M.A. Shaheen, M.F. Suleiman, Stress concentration factors of CFRP-reinforced tubular K-joints via zero point structural stress approach, *Mar. Struct.* 84 (2022) 103239, <https://doi.org/10.1016/j.marstruc.2022.103239>.
- [54] ARSEM, Design Guides For Offshore Structures - Welded tubular Joints, 1, Paris: Technip, Paris France, 1987.
- [55] P. Smedley, P. Fisher, Stress concentration factors for simple tubular joints, *Lloyd's Regist. Shipp. Heal. Saf. Exec. - Offsh. Technol. Rep. (OTH. 91. 354)* (1991) 475–483.
- [56] Recommended Practice for Planning D and CFOP-WSD. API RP 2A WSD 22nd Edition. vol. 2014, (2014), Switzerland.
- [57] H. Ahmadi, M.A. Lotfollahi-yaghin, S. Yong-bo, Experimental and numerical investigation of geometric scfs in internally ring-stiffened tubular KT-joints of offshore structures, *J. Pers. Gulf* 43 (2013) 7–8.
- [58] H. Ahmadi, E. Zavvar, Stress concentration factors induced by out-of-plane bending loads in ring-stiffened tubular KT-joints of jacket structures, *Thin-Walled. Struct.* 91 (2015) 82–95, <https://doi.org/10.1016/j.tws.2015.02.011>.
- [59] H. Ahmadi, Probabilistic analysis of the DoB in axially-loaded tubular KT-joints of offshore structures, *Appl. Ocean. Res* 87 (2019) 64–80, <https://doi.org/10.1016/j.apor.2019.03.018>.
- [60] Y. Zhang, K. Zhang, H. Zhao, J. Xin, M. Duan, Stress analysis of adhesive in a cracked steel plate repaired with CFRP, *J. Constr. Steel. Res* 145 (2018) 210–217, <https://doi.org/10.1016/j.jcsr.2018.02.029>.
- [61] H.S. Mohamed, L. Zhang, Y.B. Shao, X.S. Yang, M.A. Shaheen, M.F. Suleiman, Stress concentration factors of CFRP-reinforced tubular K-joints via zero point structural stress approach, *Mar. Struct.* 84 (2022) 103239, <https://doi.org/10.1016/j.marstruc.2022.103239>.
- [62] H. Ahmadi, E. Zavvar, Degree of bending (DoB) in offshore tubular KT-joints under the axial, in-plane bending (IPB), and out-of-plane bending (OPB) loads, *Appl. Ocean. Res.* 95 (2020) 1187–1206, <https://doi.org/10.1016/j.apor.2019.102015>.
- [63] E. Niemi, W. Fricke, S.J. Maddox, The Structural Hot-Spot Stress Approach to Fatigue Analysis, Springer, 2018, https://doi.org/10.1007/978-981-10-5568-3_2. Second Edit.
- [64] M. Iqbal, S. Karuppanan, V. Perumal, M. Ovinis, A. Khan, M. Faizan, Stress concentration factors in KT-joints subjected to complex bending loads using artificial neural networks, *Civ. Eng. J* 10 (2024) 1051–1068, <https://doi.org/10.28991/CEJ-2024-010-04-04>.
- [65] M. Iqbal, S. Karuppanan, V. Perumal, M. Ovinis, M. Iqbal, A. Rasul, Optimization of fibre orientation for composite reinforcement of circular hollow section KT-joints, *Int. J. Struct. Integr.* 15 (2024) 717–730, <https://doi.org/10.1108/IJSI-04-2024-0054>.
- [66] V.K. Ganesh, N.K. Naik, Some strength studies on FRP laminates, *Compos. Struct.* 24 (1993) 51–58, [https://doi.org/10.1016/0263-8223\(93\)90054-T](https://doi.org/10.1016/0263-8223(93)90054-T).
- [67] M. Efthymiou, Development of SCF Formulae and Generalised Influence Functions For Use in Fatigue Analysis, UEG Offshore Research, Surrey, UK, 1988.
- [68] A. N'Diaye, S. Hariri, G. Pluvinage, Z. Azari, Stress concentration factor analysis for notched welded tubular T-joints, *Int. J. Fatigue* 29 (2007) 1554–1570, <https://doi.org/10.1016/j.ijfatigue.2006.10.030>.
- [69] A. N'Diaye, S. Hariri, G. Pluvinage, Z. Azari, Stress concentration factor analysis for notched welded tubular T-joints, *Int. J. Fatigue* 29 (2007) 1554–1570, <https://doi.org/10.1016/j.ijfatigue.2006.10.030>.
- [70] H. Ahmadi, M.A. Lotfollahi-Yaghin, S. Yong-Bo, Chord-side SCF distribution of central brace in internally ring-stiffened tubular KT-joints: a geometrically parametric study, *Thin-Walled Struct.* 70 (2013) 93–105, <https://doi.org/10.1016/j.tws.2013.04.011>.
- [71] H. Ahmadi, M.A. Lotfollahi-Yaghin, Stress concentration due to in-plane bending (IPB) loads in ring-stiffened tubular KT-joints of offshore structures: parametric study and design formulation, *Appl. Ocean Res* 51 (2015) 54–66, <https://doi.org/10.1016/j.apor.2015.02.009>.
- [72] M. Rabi, F.P.V. Ferreira, I. Abarkan, V. Limbachiya, R. Shamass, Prediction of the cross-sectional capacity of cold-formed CHS using numerical modelling and machine learning, *Resul. Eng.* 17 (2023) 100902, <https://doi.org/10.1016/j.rineng.2023.100902>.
- [73] H. Ahmadi, M. Ali Lotfollahi-Yaghin, S. Yong-Bo, M.H. Aminfar, Parametric study and formulation of outer-brace geometric stress concentration factors in internally ring-stiffened tubular KT-joints of offshore structures, *Appl. Ocean Res* 38 (2012) 74–91, <https://doi.org/10.1016/j.apor.2012.07.004>.